Resource characterization of a commercial tidal stream energy site: Morlais, Irish Sea

Chisholm, Jude; Roberts, Michael; Powell, Ben; Rowlands, Steve; Robins, Peter; Roome, Edward; Hughes, Peter; Owen, Aled; Milford, Charlie; Amjadian, Pegah; Neill, Simon

Renewable Energy

DOI:
10.1016/j.renene.2025.122952

E-pub ahead of print: 01/07/2025

Peer reviewed version

Resource characterization of a commercial tidal stream energy site: Morlais, Irish Sea

Jude E. Chisholm[a,*], Michael Roberts[a], Ben Powell[a], Steven Rowlands[a], Peter Robins[a], Edward Roome[a], Peter Hughes[a], Aled Owen[a], Charlie Milford[a], Pegah Amjadian[b], Simon P. Neill[a]

[a]*School of Ocean Sciences, Bangor University, Menai Bridge, LL59 5AB, UK*
[b]*School of Civil Engineering, University College Dublin, Dublin, Ireland*

Abstract

Tidal stream energy conversion is an attractive renewable energy option due to the predictability of tides and high energy density. Yet, before sites can be exploited to their full potential, detailed resource characterization is required to optimize device selection and array configuration, and to minimize environmental impacts. This study focuses on the Morlais tidal energy site in North Wales, where developers have been awarded 38 MW of tidal stream generation capacity by the UK Government. The study analyzes sea bed and water column data collected across the site over the past decade, including multibeam echosounder data, multiple acoustic Doppler current profiler (ADCP) time series, meteorological and wave data. Additionally, high-resolution tidal and wave models are applied to further characterize the spatio-temporal variability. The undisturbed power density exceeds 10 kW/m^2 at Morlais, with the most energetic locations closest to the shore – facilitating power export to the grid. There is significant interaction of waves and currents across the site. However, this mainly influences wave properties, which could affect maintenance of moorings or devices (due to increased wave steepness), rather than directly influencing the tidal energy resource. There are variations in flood/ebb asymmetry between ADCP moorings, and this is relatively strong at some locations.

Keywords: Hydrodynamics, Tidal energy conversion, Bathymetry, Wave-current interaction, Environmental impacts, Anglesey, South Stack

*Corresponding author
Email address: jdc20v1b@bangor.ac.uk (Jude E. Chisholm)

1. Introduction

The multiple impacts of anthropogenic climate change in recent decades has prompted governments worldwide to establish emission targets on greenhouse gases [1]. Although targets vary between nations, the UK aims to achieve carbon neutrality by 2050 [2]. Renewable energy sources are an integral part of achieving these targets, providing 41.1% of UK power generation in 2023 [3]. The UK's shelf seas offer a large sea space for the expansion of the renewable energy sector (e.g. offshore wind and floating solar), as well as sources of energy not available on land including wave and tidal energy. Although the variability of power output is a drawback for all renewables, a major advantage of tidal energy is that tidal stream currents are highly predictable, and so this variability is known in advance to a high level of accuracy [4]. In addition, tidal currents possess a high energy power compared with other renewable energy resources (e.g. offshore wind), with power densities of 10 kW/m^2 not uncommon during spring tides [5].

Test sites are an essential part of TEC (tidal energy converter) development, bridging the gap between tank tests and full scale deployment [6]. Observing the behaviour of prototype devices at test sites reduces developer risk. The European Marine Energy Centre (EMEC) in Orkney, Scotland, is one such example, which has supported the development of TECs from a large number of clients, including OpenHydro and Atlantis [7]. The Marine Energy Test Area (META) is a test site in Wales, which has five quayside and three open-water berths [6].

Although tidal energy has not yet attained the same commercial success as offshore wind, steady progress is being made in the industry. This includes the MeyGen project, which in 2014, received consent to install an 86 MW array in the Inner Sound of Stroma (Pentland Firth, Scotland), where tidal flows are some of the strongest in the world (exceeding 5 m/s in some areas) [8] [9] [10]. As the environmental impacts of such an array are unknown, and to aid investment, development is taking place in three phases. The first phase (6 MW – four 1.5 MW turbines) has been operational since 2018. Having generated over 70 GWh of electricity, it has demonstrated the commercial viability of such a project. MeyGen plans to install an array totalling 398 MW at this site in the future.

Further interest in the development of tidal energy is demonstrated by the results of UK Allocation Rounds 4-6, where contracts for difference (CfD) have been awarded to eight tidal stream developers [11]. Consent for a total of 120 MW of installed tidal stream capacity has been distributed across these developers (Table 1) – 82 MW in Scotland, and 38 MW in Wales. Currently, there are no such contracted tidal stream projects in England.

Morlais (Fig. 1) is a Welsh tidal stream energy project led by Menter Môn[1] [12]. The way in which the project operates is unique. A large portion of the

[1] Menter Môn is a not-for-profit social enterprise that delivers a range of schemes throughout Wales.

required infrastructure for tidal energy extraction will be constructed at the Morlais site, at which point berths will be rented to TEC developers to install their devices while making use of the grid connection to distribute the electricity. Cable installation from the substation to the TECs is the responsibility of the developers. By exploiting the energy of the tidal stream at the Morlais site, this predictable and persistent resource will compliment the well-established but stochastic offshore wind energy industry in the Irish Sea [13]. Four developers have been awarded CfD for projects in the Morlais site, totalling approximately 38 MW of electricity ([14], [15], Table 1), i.e. all of the currently operational tidal stream in Wales. See [16] for a resource assessment of Ramsey Sound, where a TEC device is installed but not operational.

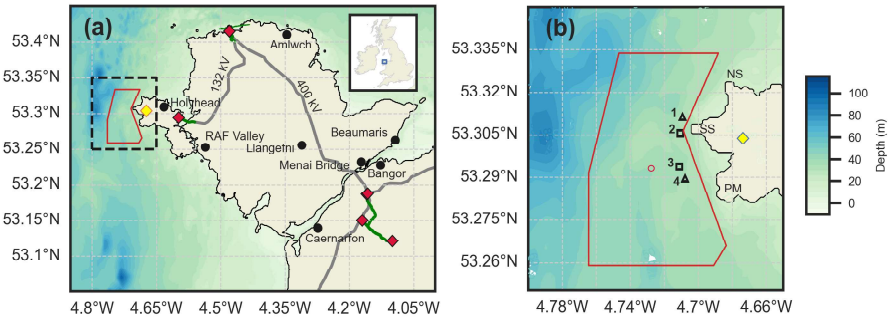

Figure 1: A map of Anglesey with the Morlais site shown as a red polygon and bathymetry shown as colour scale (in metres relative to mean sea level). Also shown are electricity substations (red=operational, yellow=under construction) and both overhead (grey) and underground (green) power lines ($\geq$ 132 kV). In (b) the locations of the four ADCP deployments are shown as black squares (4-beam) and triangles (5-beam) – see Section 3.4. The red circle in (b) (centroid of Morlais leased area) is the location that wave time series were examined over a 12 year time period – see Section 3.5. In (b) three headland regions are labelled: NS=North Stack, SS=South Stack, PM=Penrhyn Mawr.

From a previous model study of the region [17], the peak (depth-averaged) tidal currents were predicted to exceed 3 m/s towards the eastern site boundary (closest to the coastline), with simulated peak power density exceeding 20 kW/m^2 during spring tides (Fig. 2).

A range of observational data (multibeam, ADCP and wave data) has been collected over the last decade to provide a detailed characterization of the bathymetry, hydrodynamics, and wave climate of the Morlais site. The data includes four ADCP moorings that were deployed in 2023 for the present study. Additionally, high-resolution tidal and wave models are available for the region. The aim of this work is to analyze this observational and model data to produce a detailed characterization of the site's undisturbed tidal stream resource. Specifically, we focus on two research strands that are important at the site

Table 1: Tidal stream capacity (MW) awarded per Allocation Round AR4, AR5, and AR6 in Wales and Scotland.

Country	Site	Berth/Location	Location Code	Developer	AR4	AR5	AR6	Total
Wales	Morlais	Ynni'r Llcuad	SH219818	Hydrowing		10	10	20
		GO3	SH219818	Môr Energy		4.5		4.5
		BL3	SH219818	Verdant Power		4.9		4.9
		GR3	SH219818	Magallanes	5.62	3		8.62
							Total Wales	**38.02**
Scotland	MeyGen	Unspecified	Unspecified	SAE Renewables	28			56.94
		AR51	ND346749			11.8		
		AR52	ND346749			5.6		
		AR53	ND346749			2.94		
		AR54	ND346749			1.6		
		AR62	ND346749				9	
	EMEC	Unspecified	HY542313	Seastar			4	4
		Unspecified	HY542313	Ocean Star Tidal			1.5	2
		Unspecified	HY542313				0.5	
		Berth 1	HY542313	Magallanes		1.5	3	4.5
	Orkney	Eday 1	HY542313	Orbital Marine	2.4			14.4
		Eday 2	HY542313		4.8			
		Eday 3	HY542313			2.4		
		Eday 4	HY542313			4.8		
							Total Scotland	**81.84**

and at other tidal energy sites globally: wave-current interaction, and vertical variations in power density.

2. Morlais

As owners of the sea bed, The Crown Estate designated an area of 35 km^2 off the coast of Holy Island (Ynys Cybi) – part of Anglesey (Ynys Môn) – as the 'West Anglesey Demonstration Zone' in 2013 [12]. The purpose of this demonstration zone was to encourage the development of tidal energy, with funding from the Crown Estate and Nuclear Decommissioning Authority. In 2014, Menter Môn was awarded the lease for the zone and the project was renamed Morlais ('Voice of the Sea'). In 2017, the location of the substation was agreed (Fig. 1b), and construction was completed in 2023 [18][19]. Also in 2017, an application was submitted to the Welsh Government for a capacity of up to 240 MW. Consent for this was awarded in 2021, as was a marine licence from Natural Resources Wales [20]. Further funding was obtained from the EU's Regional Development Fund (ERDF) in 2022 (€37.6 million). From this point, the site is being developed in a step-by-step approach (similar to the MeyGen project in Scotland) – so that unforeseen environmental impacts can be addressed as they arise. The Environmental Monitoring and Mitigation Plan (EMMP) for the site, developed cooperatively with local stakeholders, was recently (September 2024) approved by the Welsh Government and has the purpose of preventing harm to marine wildlife during device deployments. In February 2025 the Welsh Government announced an £8M equity stake in the project. The first devices are expected to be deployed in 2026.

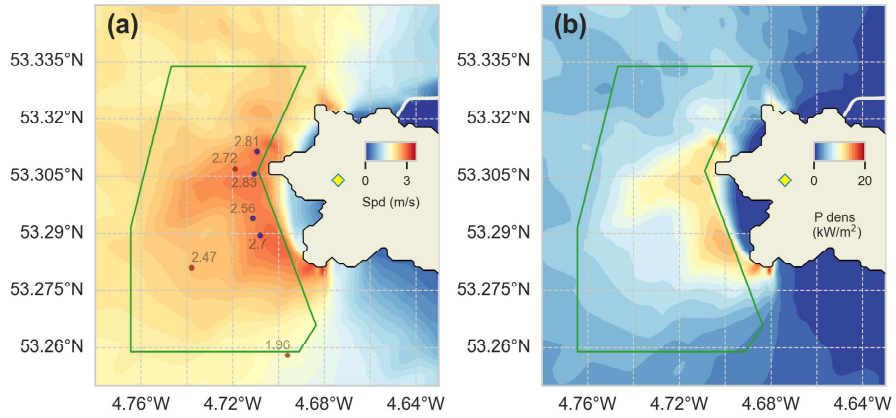

Figure 2: Simulated depth averaged peak (a) currents and (b) power density at Morlais. The values in (a) are the observed peak depth-averaged currents (in m/s) from this study and from previous ADCP deployments in the region [17] – the linear Pearson $r^2 = 0.954$ between model and observations. In (a) dark blue circles indicate ADCPs deployed for the current study, whereas historical ADCPs are coloured dark red. The yellow diamond is the location of the Morlais sub-station. The model is described in Section 3.6.

3. Methods

3.1. Multibeam Echo Sounder Surveys

Due to the specific aims of SEACAMS[2] RD&I projects, the large geographical extent of the Morlais site (35 km^2), subsequent boundary iterations (the original zone extended further to the southwest), and initial uncertainties associated with connectivity options, multibeam echosounder (MBES) surveys of Morlais were designed and undertaken using a phased approach between 2014 and 2019. Nearshore, shallow water surveys, for water depths < 20 m were conducted using a frame-mounted SeaBat 8101 multibeam system deployed through a 'moon-pool' situated on the rear deck of a 7.9 m Cheetah catamaran survey vessel. Offshore, deeper water surveys were conducted using a hull mounted SeaBat 7125 multibeam system aboard Bangor University's 35 m vessel RV Prince Madog. In both cases the MBES systems were coupled to an Applanix Wavemaster POS MV position recorder and Trimble DGPS receiver systems to account for lateral and vertical movement of the vessel. Surface and water column sound velocity values were obtained using Reson SVP70/1 and SVP15T profilers, respectively. Data were collected using frequencies in the range $240 - 300$ kHz, and the raw data processed using the Teledyne PDS2000 software package. These data were subsequently corrected for changes in tidal height, water column sound speed, and lateral positioning. Positional data was

[2]SEACAMS I and II (Sustainable Expansion of the Applied Coastal And Marine Sectors) were European Regional Development Fund projects.

referenced in the geographical coordinate system WGS84 and projected in Universal Trans Mercator (UTM) Zone 30N. All vertical elevations were reduced to mean sea level (MSL). Following these corrections, the data were exported and converted to a QPS Fledermaus bathymetric file type for detailed analysis and visualization. The resolution achieved was dependent on survey speed and water depth, and typical resolutions from the surveys from within and adjacent to the zone ranged between 0.2 to 0.5 m. Including repeat surveys to examine temporal movement of seabed sediments, approximately 100 km^2 of seabed within and immediately adjacent to the Morlais Demonstration Zone was surveyed using MBES between 2014 and 2019, including 100% coverage of the 35 km^2 of Morlais.

3.2. Meteorology

Hourly wind data were obtained from RAF Valley (Fig. 1a) – the closest synoptic meteorological station to Morlais – over a 21 year period ($2003-2023$) that covered the time period of the ADCP deployments (Section 3.4). RAF Valley is located 10 m above mean sea level, is surrounded by low lying terrain, and is fairly representative of conditions in Morlais [21].

3.3. Tidal elevations – Holyhead tide gauge and ADCP pressure sensors

Hourly tide gauge data was obtained from the British Oceanographic Data Centre (BODC) for Holyhead (53.3139N, 4.6204W, Fig. 1a) for the period of data collection of the ADCP 1 mooring initially ($26/01/2023-03/03/2023$) (Fig. 1b). The magnitude of the tidal elevation at ADCP 1 exhibited a high degree of similarity with that of the Holyhead tide gauge data. This was determined via a Pearson linear correlation test ($r = 0.994$, $n = 875$, $p < 0.001$) and a RMSE of 0.17 m (16.56% of the mean absolute value of the observations).

Having established that the Holyhead tidal gauge data is a good proxy for the observed tides at the ADCP sites, tidal gauge data from Holyhead was obtained for the 30 year period 01/01/1990 00:00 – 01/01/2020 00:00. This data exhibited a large number of gaps of varying length. The record over the period 01/01/1996 00:00 – 01/01/2005 00:00 was relatively undisturbed and provided a sufficient length to allow the MATLAB package `t_tide` to conduct tidal analysis, resolving a large range of tidal constituents with minimal error. Validation of the analysis of this 9 year period came from the high degree of similarity with that conducted with the ADCP data.

3.4. Tidal currents

ADCPs were deployed on sea bed moorings at four locations within the Morlais site, and an ensemble averaging interval of 10 minutes was applied to all ADCP data (Fig. 1b). Acoustic release pop-up buoys were used for all deployments, and so there was no surface expression from any of the moorings, e.g. surface marker buoys, to minimize impact and reduce the likelihood of entanglement with vessels passing through the area. Two of the ADCPs were equipped with a fifth (vertical) beam to measure wave properties using Acoustic

Table 2: Technical details of the four ADCP moorings.

	ADCP 1	ADCP 2	ADCP 3	ADCP 4
Latitude	53° 18.682, N	53° 18.333, N	53° 17.672, N	53° 17.372, N
Longitude	4° 42.561, W	4° 42.634, W	4° 42.584, W	4° 42.474, W
Start date	26/01/2023	20/01/2023	02/05/2023	27/04/2023
End date	03/03/2023	03/03/2023	02/07/2023	09/06/2023
Deployment length (days)	36	42	61	43
Water depth (m, relative to MSL)	38.2	39.8	35.6	33.61
Instrument	Nortek Signature 500	Teledyne RDI Workhorse Sentinel 600	Teledyne RDI Workhorse Sentinel 600	Nortek Signature 500
Number of beams	5	4	4	5
Acoustic frequency (kHz)	500	614.4	614.4	500
Blanking distance (m)	0.5	1	1	0.5
Bin size (m)	1.6	2.0	2.0	1.6
Number of bins	34	25	25	34
Sampling frequency (Hz)	4	0.42	0.42	4
Peak depth-averaged velocity (m/s)	2.81	2.83	2.56	2.70

Surface Tracking (AST) at a sampling frequency of 4 Hz (Section 3.4.2), in addition to recording currents.

3.4.1. Four beam ADCPs – currents only

A four-beam Teledyne/RDI Workhorse Sentinel 600 ADCP was deployed at two locations during two different time periods: January to March 2023 (ADCP 2), and May to July 2023 (ADCP 3) (Table 2).

Over their respective deployment periods, the depth-averaged current speed U_{mean} reached 2.83 m/s at the ADCP 2 mooring and 2.56 m/s at ADCP 3. Since these deployments were not concurrent, some of the discrepancy in peak current speed may have arisen from the phasing of various tidal constituents, however differences in velocity over small spatial scales have been found at other energetic tidal sites [22]. Although a possible contributing factor, Fig. 2a indicates that stronger current speeds have been modelled at the point where ADCP 2 was positioned – as would be expected by the proximity to South Stack (headland).

Multiple spring-neap cycles are evident and all are consistent with the degree of variability in the undisturbed water depth in both cases, which ranged between $37 - 42.6$ m at ADCP 2 and $33 - 37$ m at ADCP 3.

Four additional four-beam ADCP deployments (two within and two nearby the Morlais site) were available from a previous study of the region [17]. Although not further analyzed here, the purpose of using this data was to further resolve the spatial variability of U_{mean} across the site. The locations of the three ADCPs that were within and close to Morlais are shown in Fig. 2a along with their peak U_{mean}.

3.4.2. Five beam ADCPs – waves and currents

A further two moorings (ADCP 1 and ADCP 4) consisted of a Nortek Signature 500 (five-beam) ADCP, where the fifth (central) beam measures wave

properties using Acoustic Surface Tracking (AST). The central beam sampled at 4 Hz for 8 minutes 32 seconds (i.e. 2048 samples) every half hour. Each of these instruments was deployed during the same period as a four-beam Teledyne ADCP (Table 2). Peak depth-averaged spring current speeds of 2.7 m/s at ADCP 4 are consistent with those from the simultaneously deployed ADCP 3. ADCP 1 experienced a maximum U_{mean} of 2.81 m/s – similar to that observed at ADCP 2, validating the model outputs in Fig. 2.

3.5. Wave modelling

As mentioned in Section 3.4.2, the Nortek Signature 500 ADCPs had a vertical beam which measured surface elevations using Acoustic Surface Tracking during periods of high frequency bursts (4 Hz) every half hour, directly measuring wave-current interaction, and enabling wave statistics to be calculated such as significant wave height (H_s). However, to consider the wave climate of the site over a longer time period, a wave model was used. The model is described fully in Neill [13]; however a summary is provided here, as well as a small modification (time period extended from 10 to 12 years) compared to the original study.

The wave model was applied in two stages – initially a coarser outer grid of the North Atlantic was run, and a high resolution (curvilinear) grid of the Irish Sea was nested inside at a resolution of approximately $1/120 \times 1/202^{\circ}$ – close to 500 m. Version 41.31 of SWAN was run in third-generation mode for both model scales (outer and nested), with Komen linear wave growth and whitecapping, and quadruplet wave-wave interactions [23]. Both model configurations had spectral (directional) resolutions of 8° (i.e. 45 azimuthal directions), and discretized frequencies in the range $0.04 - 2.0$ Hz, logarithmically distributed into 40 frequency bins. Three-hourly ERA5 wind fields were used to force both models for 12 years (2012-2023)[3] at a time step of 2 minutes, with the inner nested model also forced along the boundary with hourly action density spectra from the outer model. The model was validated at four wave buoys distributed around the Irish Sea [13], and for the present study time series of H_s and energy wave period (T_e) were bilinearly interpreted at the centroid of the Morlais zone (Fig. 1b) every three hours for the full 12 years.

3.6. Tidal model

To characterize the tidal regime throughout the Morlais site, we ran two 60-day hydrodynamic simulations using TELEMAC-3D[4] – one with and one without the influence of sea surface wind stress (wind data was derived from the ERA5 global climate reanalysis [24] at $0.25^{\circ} \times 0.25^{\circ}$ resolution). Both simulations began on 15/01/2023 00:00:00. The model's unstructured grid has a 5 km resolution over the Irish Sea, and the resolution increases to 100 m over the

[3]Note that this 12 year time period is extended from the original 10 year wave model study which simulated waves from 2012-2021 [13].

[4]Development release 8.5.0-issue981

Morlais site. Five vertical layers are equally spaced using the sigma coordinate system. At the two open boundaries (St. George's Channel and North Channel), the model is forced with 22 tidal constituents from the TPXO v9.4 database (at $1/6 \times 1/6°$ resolution [25]). Model bathymetry was sourced from EMODnet 2022 (at 115 m resolution[5]) as well as detailed multibeam echosounder data in the Morlais site (see section 4.1). We configured the model to run in parallel on a high performance computer – Supercomputing Wales[6]). We parameterize bottom friction using a constant Nikurdase coefficient of 0.25, and we use the Smagorinski turbulence model.

4. Results

4.1. Sea bed characteristics

Water depths in Morlais increase from east to west, with a noticeable change at the western boundary delineated by the presence of a seabed depression further to the west known as 'Holyhead Deep' (Fig. 3a). The mean water depth across the Morlais leased region is 39.8 m, with minimum and maximum depths of 16.9 and 72.7 m, respectively (Table 3). The deepest region of Morlais is the northwest, and the shallowest relates to the large submerged sand bank that extends from South Stack into the leased area (Fig. 3b,c). The distribution of water depths within the Morlais leased area is shown in Fig. 4. Assuming that tidal stream technologies require water depths in the range $25 - 50$ m [26], around 92% of the Morlais site is suitable for current technologies (not considering other constraints such as the nature of the sea bed, distance to shore, and current speeds). The depth distribution is bi-modal, with modes centred on 35 m and 43 m. This distribution relates to the lateral extent of outcropping Precambrian rock platforms to the north and south, bounded by densely compacted glacial and late-glacial deposits. The locally strong tidal flows ensure that the shallower and irregular rocky surface, characterized by a complex series of fractures and gulleys, remains relatively devoid of sediment. The seabed surrounding the rock outcrops is generally irregular and characterized to the southwest by slightly deeper 'scour' features which reflect both the strength of the tidal regime and variable nature of glacial and post-glacial sedimentary deposits. The seabed to the southwest appears to be characterized by pronounced surface striae orientated NNW-SSE, which may relate to late glacial ice movement, iceberg scour or meltwater discharge [27]. The Morlais zone contains very few sedimentary bedforms associated with the contemporary tidal regime, apart from the large asymmetrical sand wave extending over 1 km to the north of South Stack. Compared to ambient water depths of around $35 - 40$ m, this feature has a depth of around 24 m at its crest (Fig. 3c) and generates an eddy system that can be seen in all of the ADCP time series during the ebb phase of the tidal cycle (Section 4.4).

[5] `https://emodnet.ec.europa.eu/geoviewer/`
[6] `https://www.supercomputing.wales/`

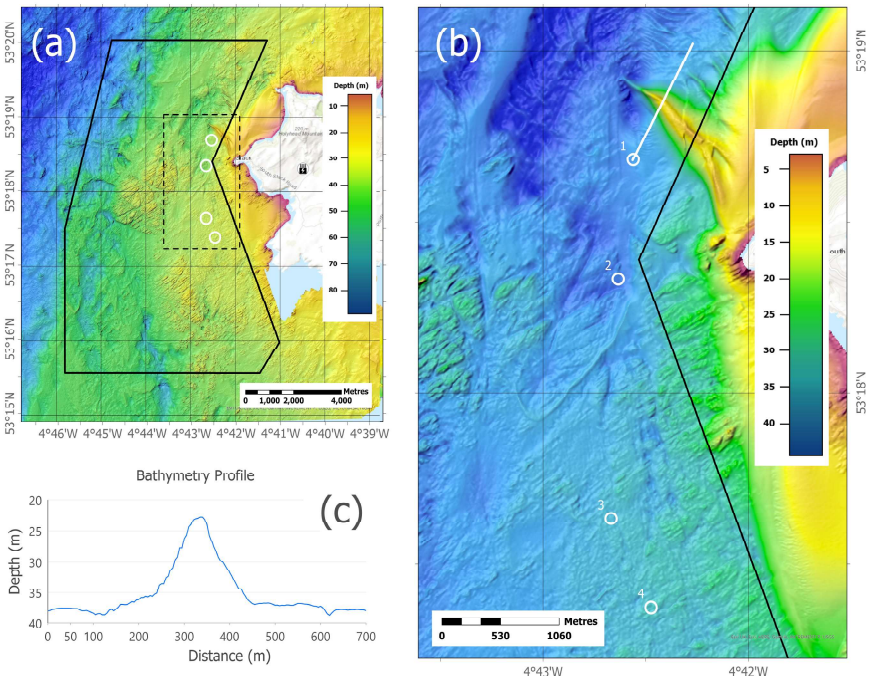

Figure 3: Bathymetry of the Morlais site interpolated to a resolution of 1 m from multiple multibeam surveys. (c) shows a profile through the large sand bank close to ADCP 1. The orientation of this profile is aligned with the tidal flow at ADCP 1 (Fig. 7a). Depths are relative to ODN (Ordnance Datum Newlyn).

Property	Depth (m)
Mean	39.8
Std	6.9
Minimum	16.9
25%	34.5
50% (Median)	38.6
75%	43.7
Maximum	72.7

Table 3: Descriptive statistics of water depths within the Morlais leased area. Std = Standard Deviation, and 25%, 50% and 75% are the first, second and third quartiles, respectively.

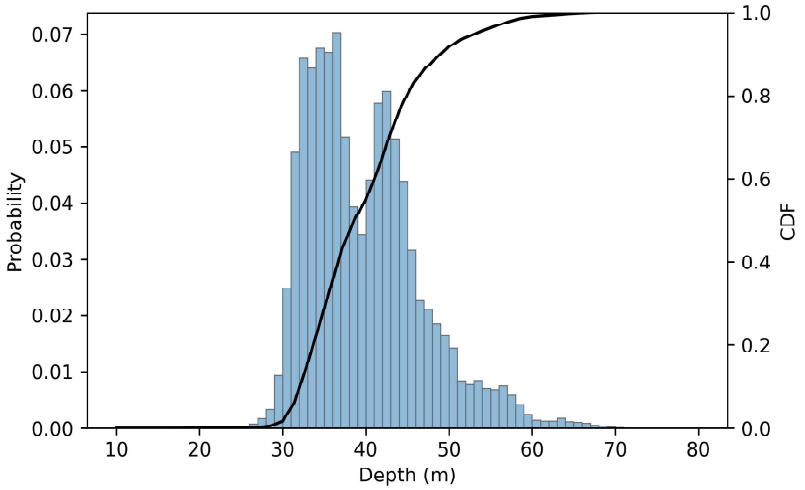

Figure 4: Distribution of water depths within the Morlais leased area shown as a probability histogram (blue boxes, left axis) and a cumulative distribution function (CDF) (black line, right axis).

4.2. Meteorology

The dominant wind direction at the Morlais site is southerly, followed by SSW and SW (Fig. 5a). The mean wind speed over the record (2003-2023) is 6.4 m/s, and the highest recorded wind speed was 26.2 m/s (SW) – wind force 10 on the Beaufort Scale ('storm'). However, the peak value of the 10 minute maximum gust wind speed in the record is 36 m/s. There is a strong diel variation in wind speed, with stronger wind speeds experienced during the day, compared to the night (Fig. 5b). The wind speeds during the ADCP deployments were relatively modest, with mean (peak) values of 6.1 m/s (12.9 m/s) (ADCP1 & ADCP2) and 4.9 m/s (11.8 m/s) (ADCP3 & ADCP4) (Fig. 5c).

4.3. Tidal elevations

The results of the `t_tide` tidal analysis are presented in Table 4, where the nature of the tide in this region can be seen to be strongly semi-diurnal, with a Form Factor $F = (K1+O1)/(M2+S2) = 0.09$ [28]. The N2 and L2 constituents together describe the varying lunar distance due to the elliptical orbital path of the Moon around the Earth – this is discussed in more detail within the context of tidal currents in Section 4.4. The relatively large K2 constituent (amplitude of around 10% of M2) further emphasises the semi-diurnal nature of the tides in this region. The Solar Annual constituent (SA) has the largest error associated with the tidal analysis (0.02 m or 22%) due to the length of record used (9 years). Although the magnitude of this long period (1 year) constituent is small

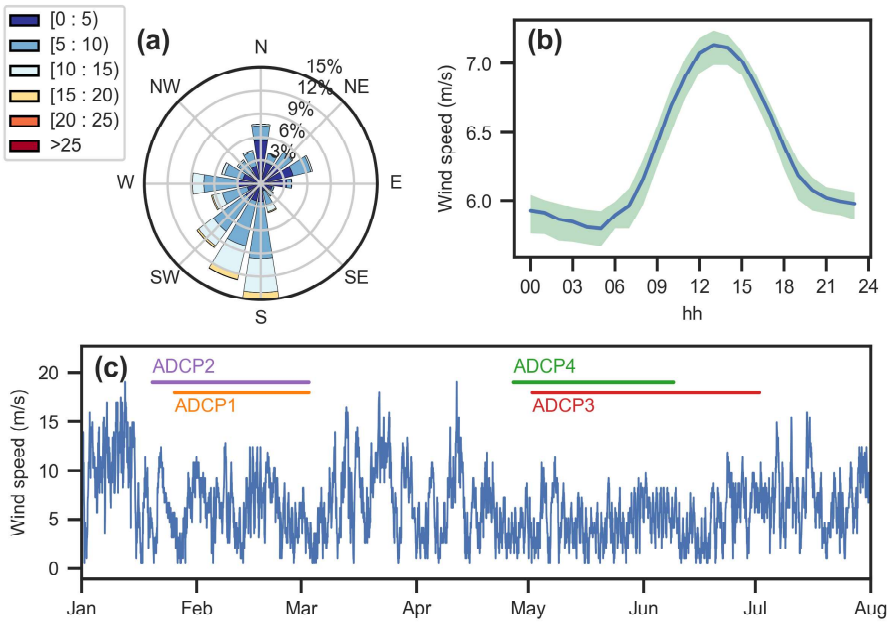

Figure 5: Wind conditions at Valley, the neighbouring synoptic meteorological station. (a) is the windrose over a 21 year period (2003-2023), and (b) is the mean diel variability in wind speed over the same time period – the blue line is the mean, and the green shading indicates the 10th and 90th percentiles. (c) shows the wind speed during the time of the ADCP deployments (marked as horizontal bars).

Table 4: The 10 largest tidal constituents (listed in descending order of amplitude) at the Morlais site, calculated using nine years of hourly tide gauge data from Holyhead – an accurate proxy for Morlais (Section 3.3). Also included on the table are the estimated errors from the `t_tide` analysis.

Constituent	Description	Period (h)	Amplitude (m)	Phase (°)	Amplitude error (m)	Phase error (°)
M2	Principal lunar semidiurnal	12.42	1.79	291.19	0.00	0.08
S2	Principal solar semidiurnal	12.00	0.59	328.61	0.00	0.26
N2	Larger lunar elliptic semi diurnal	12.66	0.36	266.20	0.00	0.37
K2	Lunisolar semi diurnal	11.97	0.18	322.39	0.00	0.96
K1	Lunisolar diurnal	23.93	0.11	174.01	0.00	1.46
O1	Lunar diurnal	25.82	0.10	32.91	0.00	1.79
SA	Solar annual	8766.23	0.09	319.71	0.02	14.58
NU2	Larger lunar evectional	12.63	0.08	272.99	0.00	1.85
L2	Smaller lunar elliptic semi diurnal	12.19	0.06	322.91	0.00	2.26
2N2	Lunar elliptic semi-diurnal second-order	12.91	0.04	241.84	0.00	2.97

(0.09 m), this error could be reduced by considering a longer time series, since it is influenced by seasonal variations in the climate [29].

4.4. Tidal currents and tidal power density

The variation in current speed for one of the ADCP time series – ADCP 4 – is shown in detail in Fig. 6, along with the variation in surface elevations. The difference in magnitude between the flood and ebb phases of the tidal cycle is very prominent.

The depth-averaged eastward and northward components of the current velocity for all ADCP moorings are plotted in Fig. 7, allowing for a comparison of the direction, magnitude and variability of the tidal currents between locations. All locations were strongly rectilinear, but all of the ADCP time series were associated with secondary flows at the beginning of the ebb phase of the tidal cycle. Although further evidence would be required to determine the cause conclusively, it is likely that these secondary flows are associated with eddies that form at the beginning of the ebb phase of the tidal cycle. While such eddies may be generated by a tidal current passing a headland [30], the location of the large sand bank to the north of ADCP 1 (Fig. 3b,c) suggests that it may lead to the formation of an eddy system during the ebb. However, since the currents

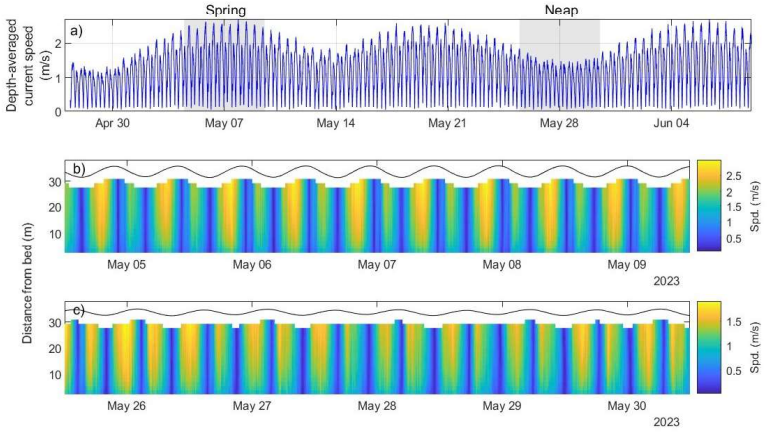

Figure 6: The variability of current speed with depth and time at ADCP 4 during a spring (b) and neap (c) phase. The black line represents the total water depth measured with the ADCP pressure sensor. ADCP 4 was plotted alone to prevent repetition, while highlighting the asymmetry of the site - most notable at this mooring.

have a relatively low magnitude (< 1 m/s) at this time, the secondary flows are unlikely to pose a problem for tidal energy extraction.

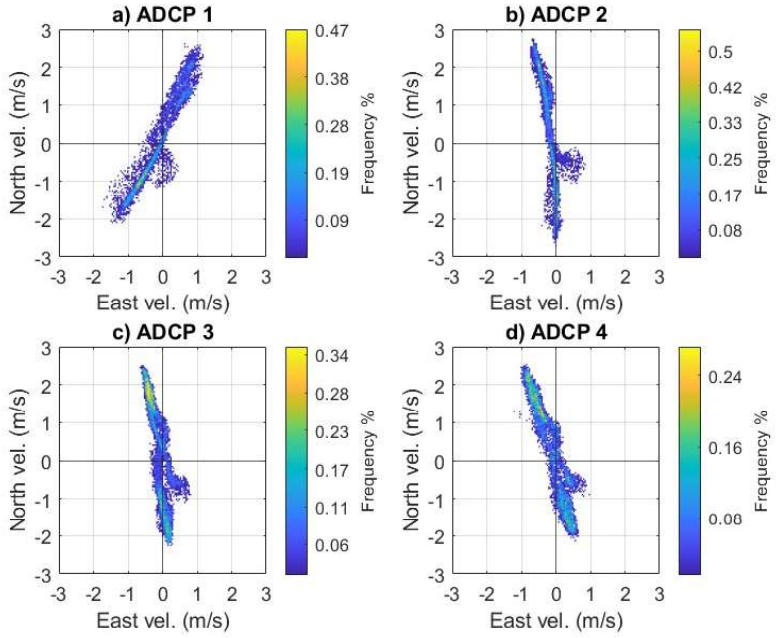

Figure 7: Scatter plots of the depth-averaged east and north components of velocity at each mooring. Positive values of the North velocity indicate the flood phase of the tidal cycle.

At the most northerly mooring (ADCP 1), during peak spring periods, U_{mean} approached 3 m/s (Fig. 8). As will be discussed later in this section, successive spring/neap cycles are modulated by the N2 and L2 tidal constituents which describe the Moon's elliptical orbit around the Earth. The largest spring currents possessed a power density of around 10 kW/m^2, while the neap tidal currents reached approximately 2 kW/m^2. A large degree of tidal asymmetry is exhibited in U_{mean}, and is exaggerated in the depth-averaged power density (P_{mean}) since it is a function of speed cubed.

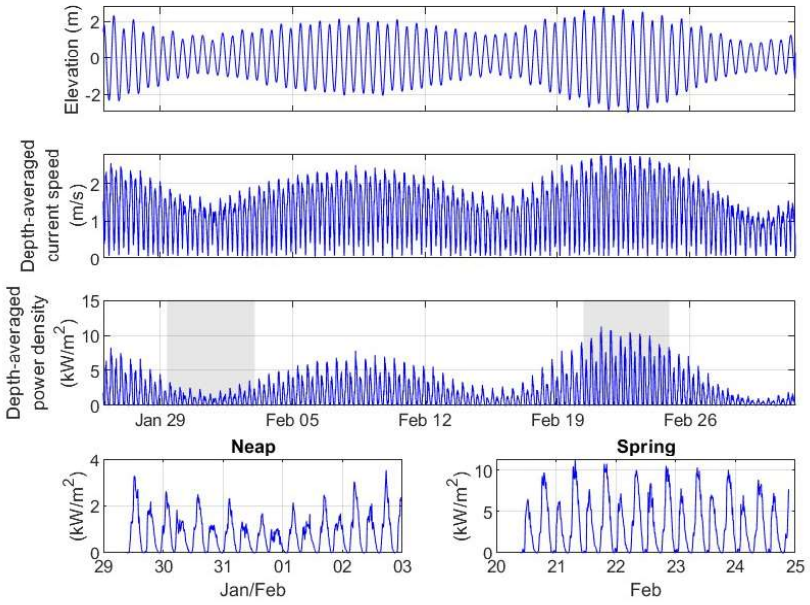

Figure 8: A time series of surface elevation, U_{mean} and P_{mean} for ADCP 1.

At ADCP 2, U_{mean} was similar to ADCP 1, approaching 3 m/s during peak springs (Fig. 8). The tidal asymmetry is less notable in this time series.

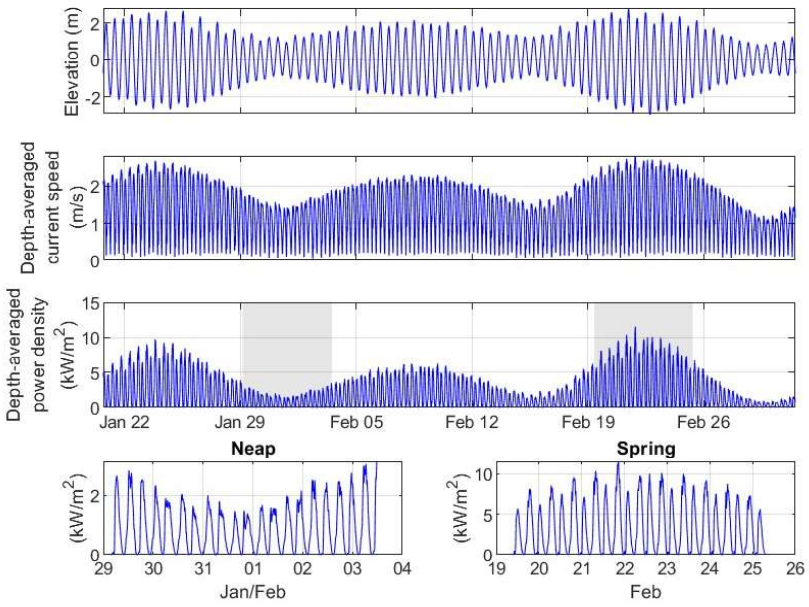

Figure 9: A time series of surface elevation, U_{mean} and P_{mean} for ADCP 2.

At ADCP 3, U_{mean} peaked at approximately 2.5 m/s, with a corresponding power density of 8.0 kW/m^2. During neaps, peak tidal currents (approx. 1.5 m/s) had a power density of around 1.7 kW/m^2. A large degree of tidal asymmetry is evident from Fig. 10.

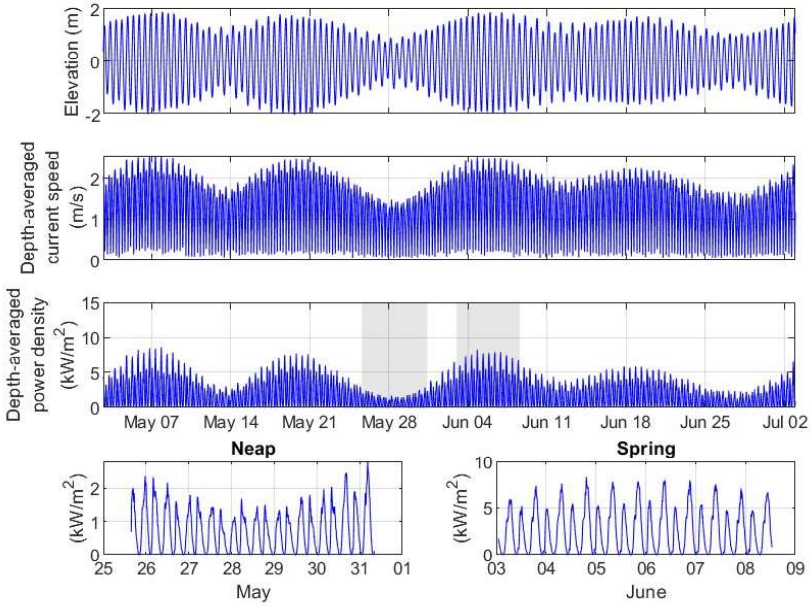

Figure 10: A time series of surface elevation, U_{mean} and P_{mean} for ADCP 3.

At ADCP 4, the tidal asymmetry is greatest, resulting in the flood tide that has a power density approximately twice that of the ebb during spring periods (where the current speed asymmetry is exaggerated). During spring periods, the current speed peaked at around 2.7 m/s, with a power density of approximately 10 kW/m^2.

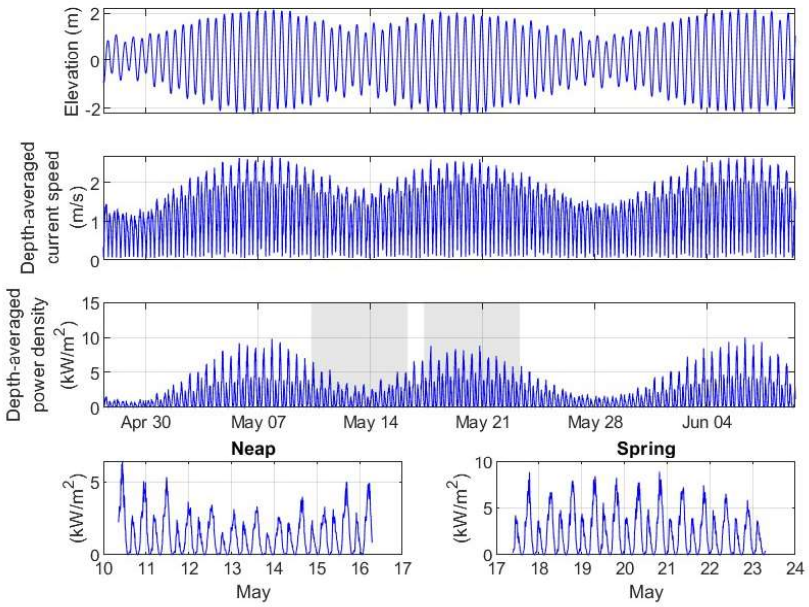

Figure 11: A time series of surface elevation, U_{mean} and P_{mean} for ADCP 4.

Within a lunar synodic period (29.53 days) there are varying magnitudes in the observed time series between the sets of spring elevations and currents. For example, at ADCP1 (Fig. 8) the spring tides around 8 February have a range of 4.12 m, whereas the spring tides two weeks later (22 February) have a range of 5.62 m. The corresponding peak spring currents for these two time periods are 2.48 and 2.80 m/s, respectively. This difference is due to the varying lunar distance, i.e. the distance between the centre of the Moon and the centre of the Earth. The orbital path of the moon around the Earth is elliptical. The point in the Moon's orbit where it is closest to the Earth is called lunar perigee, while its furthest approach is known as lunar apogee. The lunar distance is on average around 385,000 km. This reduces to around 360,000 km (perigee) and increases to 405,000 km (apogee), hence the variations in the tidal force resulting in changes in the tidal range and current speeds. Since tidal power is related to current speed cubed, the variations in peak spring power density (for example at ADCP 1) can be as much as 40%. This can be an important consideration in site selection and grid integration, as well as the length of ADCP deployment and model simulation. The variations in lunar distance are described by the N2 and L2 constituents (Table 5), noting that the semi-major axis of the N2, in particular, is around 60% that of the S2. The final constituent listed in Table

Table 5: Comparison of modelled and observed depth-averaged tidal ellipse parameters for the four ADCP locations.

Const.	ADCP	Observed				Modelled				Difference (mod-obs)			
		Semi-major axis (m/s)	Semi-minor axis (m/s)	Inc. (°)	Phase (°)	Semi-major axis (m/s)	Semi-minor axis (m/s)	Inc. (°)	Phase (°)	Semi-major axis (m/s)	Semi-minor axis (m/s)	Inc. (°)	Phase (°)
M2	1	1.79	0.081	62.9	198.9	1.87	0.106	79.5	203.4	0.08	0.024	16.7	4.6
	2	1.82	-0.021	97.4	203.5	1.80	0.016	103.8	212.4	-0.02	0.037	6.4	8.9
	3	1.86	-0.042	98.6	210.7	1.88	0.018	86.0	206.7	0.02	0.060	-12.6	-4.0
	4	1.78	-0.005	107.8	210.8	1.79	-0.003	96.7	212.9	0.02	0.002	-11.0	2.1
S2	1	0.63	0.027	63.0	257.2	0.63	0.040	79.9	260.6	0.01	0.013	16.9	3.4
	2	0.62	-0.012	97.3	262.4	0.62	0.001	103.2	268.7	0.00	0.012	5.9	6.2
	3	0.42	-0.008	98.2	237.2	0.64	0.013	86.1	263.8	0.22	0.021	-12.0	26.6
	4	0.49	0.003	107.4	232.3	0.62	-0.002	96.4	269.2	0.13	-0.005	-11.0	36.9
N2	1	0.38	0.008	64.1	165.7	0.41	0.024	79.6	170.0	0.03	0.015	15.4	4.3
	2	0.39	0.000	98.8	171.3	0.40	0.002	103.8	179.0	0.01	0.003	5.1	7.6
	3	0.26	-0.003	97.7	192.8	0.41	0.005	85.9	173.3	0.15	0.007	-11.8	-19.5
	4	0.23	-0.001	107.3	186.0	0.40	-0.001	96.8	179.6	0.17	-0.001	-10.5	-6.4
L2	1	0.16	0.011	62.1	230.9	0.17	0.006	78.1	248.8	0.01	-0.005	16.0	17.9
	2	0.16	0.005	95.6	231.0	0.16	0.001	105.6	260.2	-0.01	-0.004	10.0	29.2
	3	0.12	0.001	100.5	224.7	0.16	-0.004	85.3	252.3	0.04	-0.004	-15.2	27.7
	4	0.09	0.000	107.9	228.7	0.15	-0.003	97.7	260.9	0.06	-0.002	-10.3	32.2
M4	1	0.10	0.005	108.9	84.1	0.17	0.001	86.5	118.8	0.07	-0.004	-22.4	34.7
	2	0.07	-0.065	152.8	106.3	0.12	-0.024	135.4	156.6	0.05	0.041	-17.5	50.3
	3	0.12	-0.083	162.9	136.5	0.16	-0.012	95.0	133.8	0.04	0.071	-67.9	-2.6
	4	0.12	-0.083	173.0	143.4	0.14	-0.020	124.2	149.4	0.01	0.063	-48.8	6.0

5 is M4 – this constituent, along with M2, describes the flood/ebb asymmetry that can be seen at most of the ADCP locations (e.g. Fig. 7) [17, 31].

For completeness, and although not further discussed here, probability histograms of the depth-averaged current speeds from the four ADCP moorings are plotted in Fig. A.20.

4.4.1. Hydrodynamic model

In addition to the simulated spatial distribution of peak U_{mean} and peak P_{mean} (Fig. 2), time series of depth-averaged velocity were extracted from the 3D hydrodynamic model at the locations of the four ADCP locations (the simulation without wind stress was used). The `t_tide` tidal analysis of the model and ADCP depth-averaged velocity data are shown in Table 5 as ellipse components, including their error. The agreement between model and ADCP data is generally very good, for example the root-mean-square-error (RMSE) along the semi-major axis is 0.043 m/s for M2 and 0.128 m/s for S2, noting that the mean values are 1.81 m/s and 0.54 m/s, respectively. It is clear from Table 5 that the semi-diurnal constituents dominate (particularly M2 and S2), and that all four locations are strongly rectilinear.

From the 3D simulation (without wind stress), monthly-mean and maximum power density maps were calculated for the study region, using both sea surface and mid-depth simulated velocities (Fig. 12). At the sea surface, monthly-mean power densities reached 1.5–1.9 kW/m^2 in the more energetic eastern region of the Morlais site, whereas peak power densities reached 17.5 kW/m^2 (Fig. 12a-b). At mid-depth, monthly-mean power densities reached 1–1.5 kW/m^2, whereas peak power densities reached 14 kW/m^2 (Fig. 12c-d). At the most energetic location, 1 km northeast of Holy Island (-4.705, 53.313), simulated time series of power densities illustrated the variability over the 30-day simulation, reaching 1.2 kW/m^2 (mid-depth) and 1..4 kW/m^2 (sea surface) during neap flood tides and increasing to 14.7 kW/m^2 (mid-depth) and 17.7 kW/m^2 (sea surface)

during spring flood tides, with noticeable tidal asymmetries (i.e., up to 20% weaker power densities during the ebb phase) (Fig. 12e). We also compared the simulations with and without wind stress, and found only small differences in sea surface velocities (of order 1 cm/s), hence these results are not shown.

4.4.2. Current profile analysis

Mean (10-minute average) current profiles are presented in Fig. 13, where the tidal asymmetry can observed for each mooring (particularly during spring phases). The following empirical relation was determined by Soulsby [32] to describe the velocity profile of a tidal flow

$$U(z) = \left(\frac{z}{\beta h}\right)^{\frac{1}{\alpha}} U_{mean}, \qquad \text{for } 0 < \text{z} < 0.5\text{h} \tag{1a}$$

$$U(z) = 1.07 U_{mean}, \qquad \text{for } 0.5\text{h} < \text{z} < \text{h} \tag{1b}$$

where β and α are constants relating to friction and horizontal shear respectively, U_{mean} is the depth-averaged current speed, h is the water depth, and z is the distance from the bed. Commonly, $\beta = 0.32$ and $\alpha = 7$ (i.e. a 1/7 power law).

It was found at an early stage that using Eq. 1a alone, extended to the full depth of the water column, provided the best fit with the observations. Other work has also neglected Eq. 1b [33].

Curve-fitting software was used to determine the values of both constants for each time step via a least-squares-fit approach, and they are presented in Table 6. The methodology used was similar to that presented in Lewis et al. [33]. α was allowed to range from 1 to 20 and β from 0.1 to 2. For context, a series of fits are presented in Fig. 14. Apart from ensuring that two fits corresponded to peak flood conditions and two to peak ebb, those presented were chosen randomly. The mean values of α largely deviated from the classical 1/7 power law, often indicating greater horizontal shear ($\alpha < 7$) although not always. This is to be expected at coastal regions possessing large current speeds. At ADCPs 1 and 2, there was a notable difference in the average horizontal shear between the flood and ebb stages. For ADCP 1, the ebb had greater shear, however for ADCP 2 it was the flood, while the ebb experienced the least of all the moorings ($\alpha = 10.67$). In the case of ADCPs 3 and 4, there were only minor differences between the flood and ebb stages. In all cases, β was calculated to be 0.4, and experienced minimal deviation.

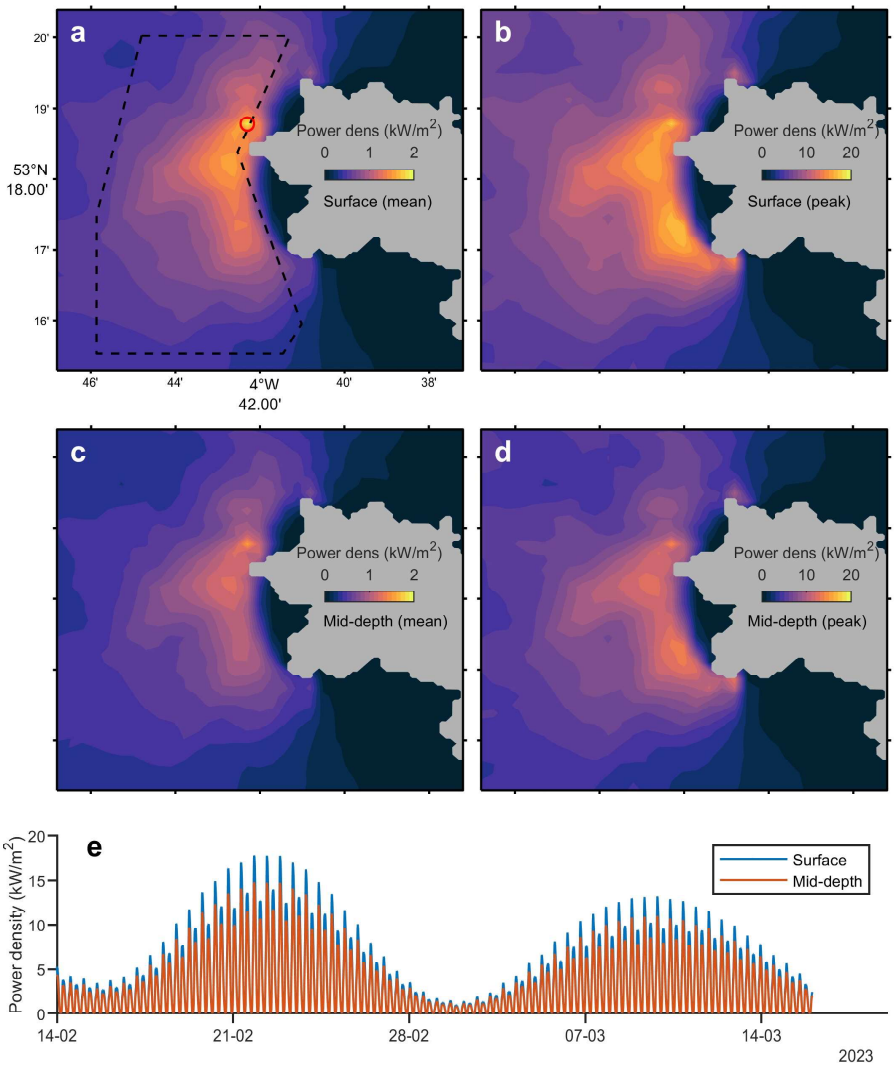

Figure 12: Simulated mean (a,c) and peak (b,d) power density over the 60 day Telemac simulation at the surface (a,b) and at mid-depth (c,d). (e) A 30 day timeseries showing surface and mid-depth power density, the location of the timeseries is marked by the red circle in (a). The lease area is delineated by the dashed black line (a).

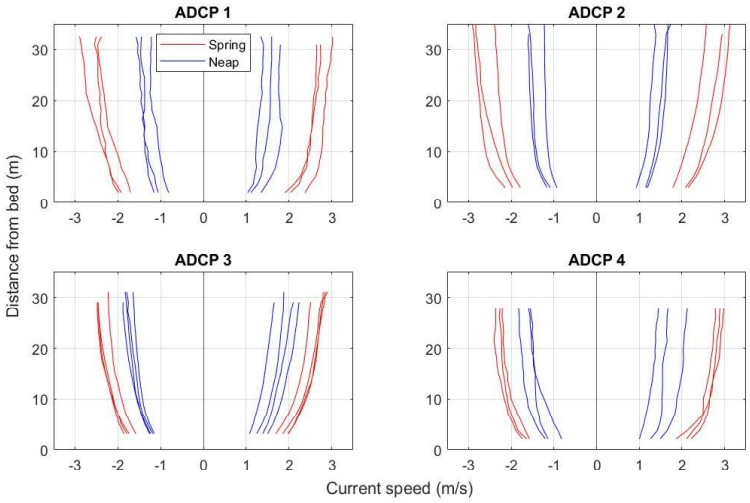

Figure 13: Current speed profiles of peak flood (positive current speed) and peak ebb (negative) points at each mooring for all spring/neap periods.

ADCP	Tidal phase	Mean α	Std α	Mean β	Std β	Mean AES	Std AES
1	Flood	8.24	1.97	0.4	<0.01	0.03	0.02
	Ebb	6.74	1.51	0.4	<0.01	0.06	0.04
2	Flood	7.58	1.64	0.4	<0.01	0.06	0.07
	Ebb	10.67	3.45	0.4	<0.01	0.04	0.04
3	Flood	5.8	0.67	0.4	<0.01	0.01	0.02
	Ebb	5.86	0.64	0.4	<0.01	0.01	0.01
4	Flood	6.4	1.29	0.4	<0.01	0.04	0.02
	Ebb	5.92	1.44	0.4	<0.01	0.03	0.02

Table 6: Statistical results of the power-law analysis. Note that the smaller the value for α, the greater the vertical shear throughout the water column. The AES is the absolute error squared.

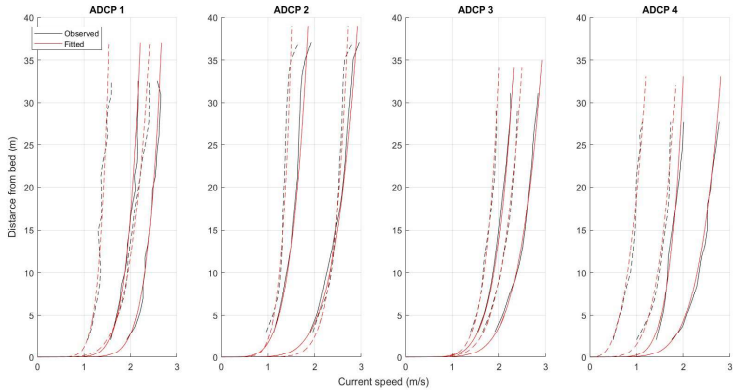

Figure 14: A selection of profiles representative of the mean AES (not permitted to deviate by more than 0.01 from this value) for each ADCP. The AES was calculated as discussed in Lewis et al. [33]. For each, two profiles are presented for peak flood tides (solid lines) and two for peak ebb tides (dashed lines). The variability in the total height of the profiles is a result of the varying depths in which the ADCPs were deployed.

4.5. Waves – shorter time scale wave properties

The dispersion relation for ocean surface waves is

$$\sigma^2 = gk \tanh(kh) \tag{2}$$

where σ is the intrinsic angular frequency, g the gravitational acceleration, k the wavenumber, and h the water depth. In regions with a significant current, however, the absolute (angular) frequency ω (that observed from a stationary device) is Doppler-shifted [32][34]

$$\omega = \sigma + ku_x \tag{3}$$

where u_x represents the components of the current velocity in the direction of wave propagation. This is calculated using $u_x = \boldsymbol{u} \cos\theta$, where θ is the angle between the direction of wave propagation and the current.

In the processing of the wave data, each measured (absolute) wave frequency spectra was therefore corrected for the Doppler-shift using the relation

$$(\omega - ku_x)^2 = gk \tanh(kh) \tag{4}$$

to determine the intrinsic wavenumber, followed by the classical dispersion relation to calculate the intrinsic frequency.

Wave properties differed significantly between the ADCP 1 and ADCP 4 moorings due to seasonal variability (Fig. 5c), but both exhibited a high degree of modulation by the tidal currents.

This is due to a form of wave-current interaction (WCI) whereby the height and length of a wave is altered when it propagates over spatial gradients of current velocity [35]. If a wave propagates with a current that accelerates with distance 'downstream', the wavelength (and thus wave period) will increase. As a consequence, the wave height reduces to conserve the rate of energy propagation. Note that the same effect would be observed if an opposing current reduced in magnitude with distance 'downstream', highlighting that it is relative changes in current speed that are important for this process. The opposite occurs when either (a) an opposing current increases or (b) a following current reduces in magnitude downstream, in which case the wave height must increase due to wave action conservation. Note also that only components of the current velocity vector aligned with the direction of wave propagation are relevant to this process. Any perpendicular motion has no effect.

This change in wave steepness, in particular, can lead to fairly uncomfortable conditions when waves and currents are opposing, even in otherwise relatively quiescent conditions, affecting the quality of data collection and the servicing of instruments or energy devices. This is confirmed by the authors over many years of fieldwork in this region.

At ADCP 1, deployed over the winter months of January-February, the average significant wave height (H_s) was 1.4 m and the average mean wave period (T_m) 4.4 s (Fig. 15). There were two broad durations of increased H_s and T_m, one between $26/01/2023 - 08/02/2023$, and the other $12 - 27$ Feb 2023. The level of wave power followed the two broad peaks, and averaged 5.5 kW/m. The significant steepness S_s parameter (bottom panel of Fig. 15) provides a statistical measure of the steepness of the wave field and is useful in examining the form of WCI previously discussed. It is defined as follows

$$S_S = \frac{2\pi H_S}{g T_m^2} \tag{5}$$

where g is the gravitational acceleration.

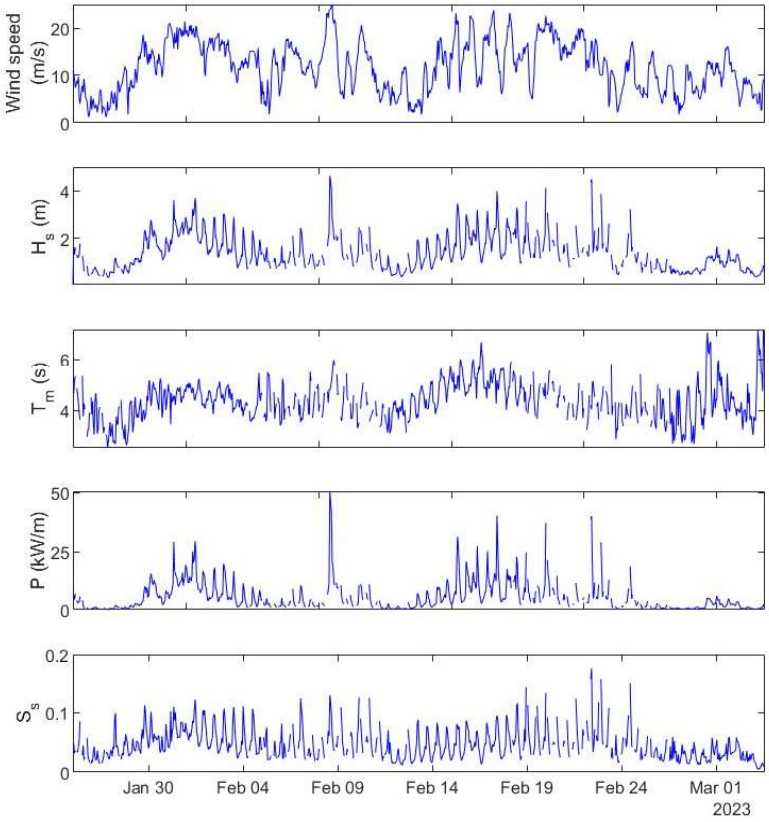

Figure 15: Wind speed (obtained from Valley, as in 5), significant wave height H_s, mean wave period T_m, wave power P and significant steepness S_s at ADCP 1 over the period 26/01/2023 - 03/03/2023. Erroneous data-points were removed during data processing and account for the small gaps in the datasets.

There was a peak in wave height on 08/02/2023 at approximately 14:00, coinciding with a tidal cycle where the asymmetry was noticeably enhanced (Fig. 8). This peak appears to have arisen from increased wind speeds alone, as it was not accompanied by a dramatic change in wind direction (Fig. 15).

At ADCP 4, the mean H_s was 0.9 m and the mean T_m 3.0 s, noting that this deployment took place from May-June. There were four very brief periods of increased H_s, the first three occurring between 04-12 May and the final between

22-24 May. A small peak occurred on 15 May. The level of wave power averaged at a relatively low 1.6 kW/m.

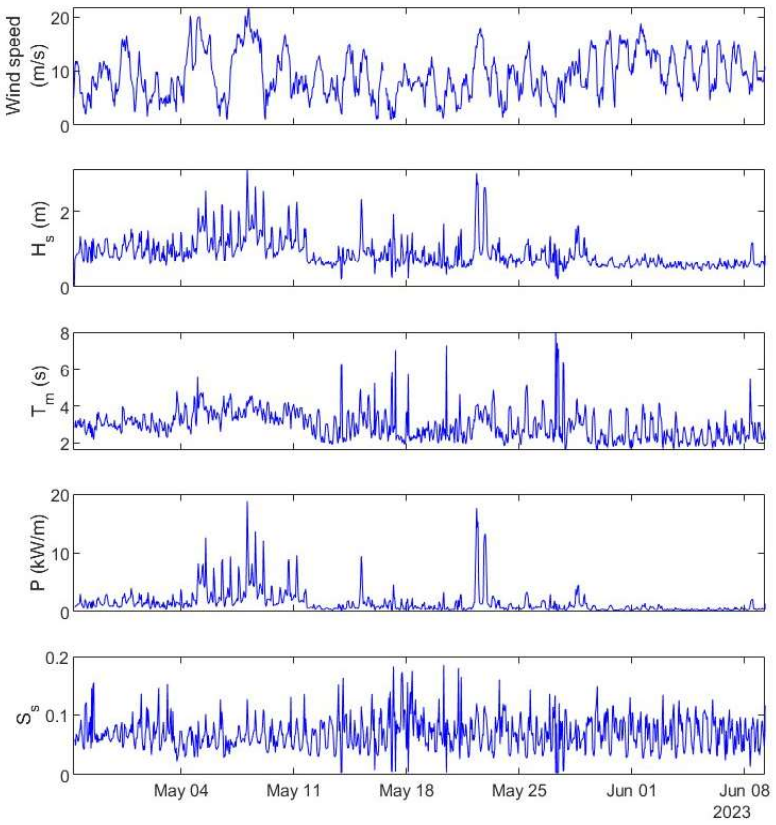

Figure 16: Wind speed, significant wave height H_s, mean wave period T_m, wave power P and significant steepness S_s at ADCP 4 over the period 27 April - 9 June 2023.

Fig. 17a highlights that the S_s at both moorings was modulated primarily at the semi-diurnal frequency (period 12.42 hours). At ADCP 4, there was a small peak in spectral energy at a period of 6.20 hours, indicating that a small amount of the modulation of the S_s can be explained by the M_4 tidal constituent (Table 5). At both moorings, S_s demonstrated the expected response to a current, reducing when the wave and current direction were aligned and increasing when

opposed. Notable, is that the S_s at ADCP 4, during the less energetic summer period, was generally larger than that at ADCP 1 (Fig. 17b).

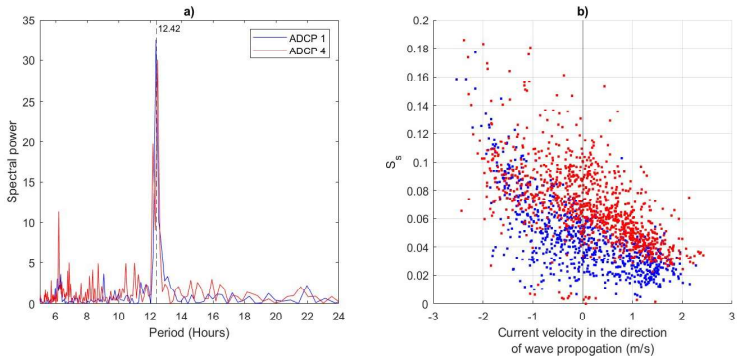

Figure 17: Fourier analysis showing the periods at which the significant steepness S_s was modulated at both ADCP/wave moorings (a) and the response of S_s to the component of the current velocity in the direction of wave propagation (b).

4.6. Waves – longer timescale wave statistics

Wave time series were output from the model described in Section 3.5 at the centroid of the Morlais leased area (Fig. 1b), noting that there was modest variation in wave properties across the site, and so waves at this location are generally representative of the entire site [13]. Over the 12 years of wave model output (2012-2023) the joint variability of significant wave height (H_s) and energy wave period (T_e) is shown in Fig. 18, and a summary of the wave statistics provided in Table 7. The maximum value of H_s = 6.64 m (corresponding T_e = 10.90 s) occurred on 16th October 2017 when the wind speed exceeded 26 m/s from the south, with a 10 minute maximum gust of 36 m/s (70 knots). However, the maximum value of T_e = 13.08 s (H_s = 1.53 m, i.e. swell) occurred during a fairly calm period on the 1st February 2021 when wind speed was around 4 m/s, again from the south.

	H_s (m)	T_e (s)
Mean	1.08	5.03
Std	0.80	1.55
25%	0.48	3.90
50% (median)	0.86	4.89
75%	1.48	6.08
Maximum	6.64	13.08

Table 7: Summary of modelled wave statistics at Morlais, 2012-2023.

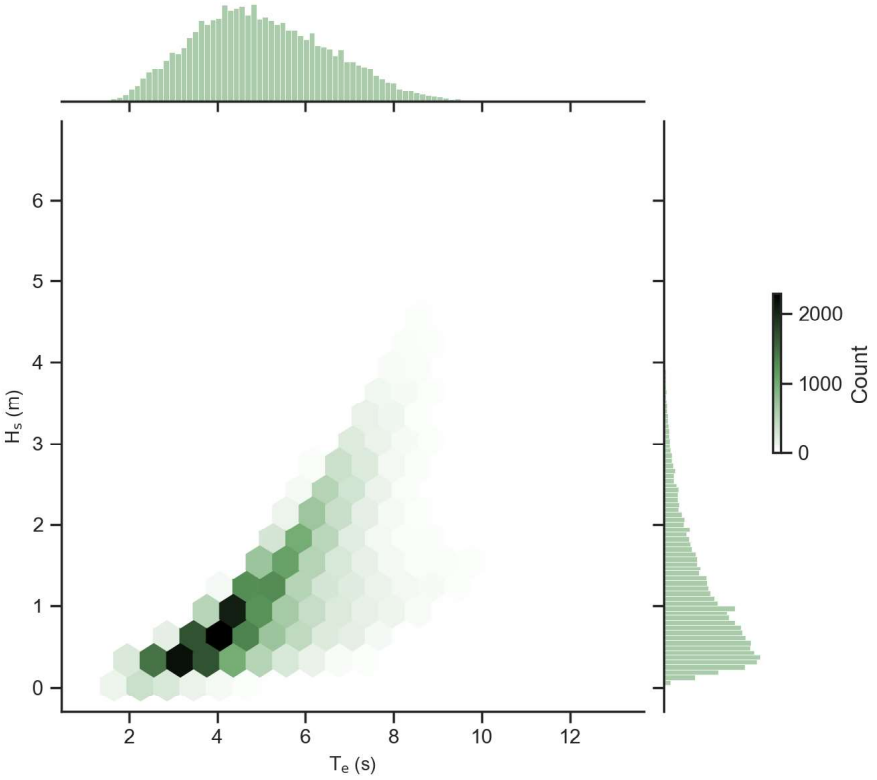

Figure 18: Simulated joint distribution of T_e and H_s at the centroid of the Morlais leased area over the 12 year period 2012-2023. The resolution is 3-hourly, and so there are a total of 35,064 records. Therefore, a count of 2,000 on the color scale represents around 5.7%.

5. Discussion

There is a degree of spatial variability in the depth-averaged power density, P_{mean}, across the observations (Table 8). The regions of Morlais close to one of two adjacent headlands (South Stack and Penrhyn Mawr – labelled on Fig. 1b) experience a greater P_{mean}, owing to localized enhancement of the tidal currents [36]. This is summarized in Table 8, where ADCPs 1 and 2 possess a greater peak P_{mean} than the other two moorings. Considering only positioning relative to a headland, ADCP 4 experiences an unexpectedly high peak P_{mean}. Examination of Fig. 11 shows that this magnitude is reached only during the flood phase, and that there is a considerable degree of asymmetry in P_{mean} (often doubling that of the ebb during the spring flood).

ADCP	Peak P_{mean} (kW/m^2)	Average P_{mean} (kW/m^2)	Average spring peak P_{mean} (kW/m^2)	Peak U_{mean} (kW/m^2)	Average U_{mean} (kW/m^2)
1	11.37	1.73	5.36	2.81	1.23
2	11.62	1.90	6.08	2.83	1.23
3	8.60	1.76	5.11	2.56	1.27
4	10.09	1.79	4.92	2.70	1.29

Table 8: The peak and average depth-averaged power density P_{mean} at each ADCP. In the process of obtaining the latter, it was ensured that the averaging took place over a lunar synodic period. The average spring peak P_{mean} is the mean peak power density during spring periods alone. Tidal asymmetry contributed to a significant reduction in this value. The maximum and average values of U_{mean} are also included in the table.

The strong tidal currents at Morlais lead to a P_{mean} that is comparable to some of the more established tidal energy regions. The average P_{mean} during peak spring tides at EMEC (Fall of Warness, Orkney) has some spatial variability. The region generally reaches 8 kW/m^2 and exceeds 10 kW/m^2 in a limited area [5]. During spring tides at the Inner Sound of the Pentland Firth, this value reaches 10 kW/m^2 over a large area [37]. It is also notable that the Fall of Warness exhibits a similar level of tidal asymmetry to that observed at Morlais [31]. At the neighbouring Anglesey Skerries, the peak power density reaches 26 kW/m^2 due to peak depth-averaged tidal currents of up to 3.7 m/s, although over a much smaller area than Morlais [38].

5.1. Power attenuation with depth

Where relatively shallow coastal flows ($h < 50$ m) reach a significant current speed, vertical shear may be present (to a varying degree) throughout the entire water column (e.g. Fig. 13). This is important for tidal energy conversion since the relationship between current speed and power density is non-linear. This section therefore seeks to examine the way in which power density varies with depth at ADCPs 1 and 4. The analysis is restricted to only these deployments to prevent repetition and cover the largest available spatial range (a reasonable contrast in depth, tidal asymmetry and current speed is also obtained in the selection of these two moorings).

Fig. 19 provides a comparison between the mean power over each tidal cycle and that at the depths examined. The disproportionately large increase in power density due to increased current speed is demonstrated in Fig. 19a, where there is a much narrower range in power density with depth during periods of neap tides.

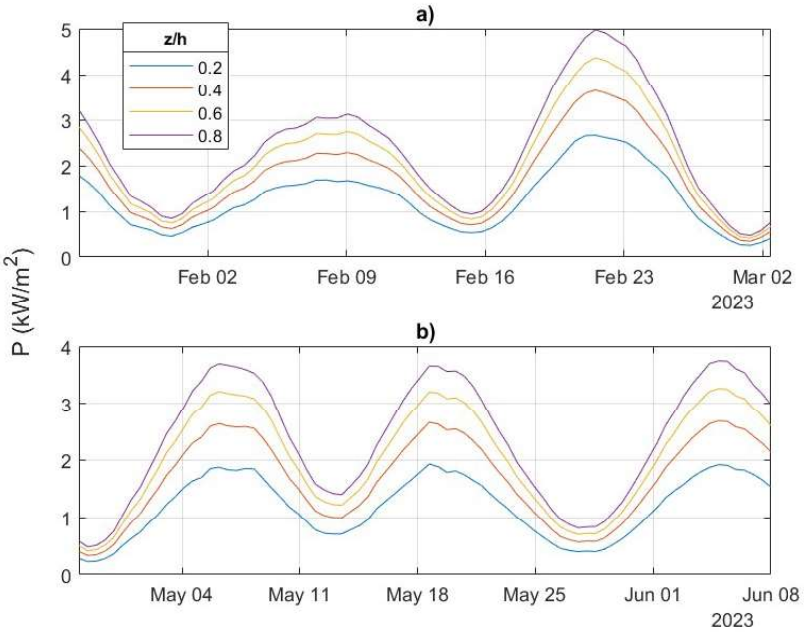

Figure 19: Examination of the attenuation of power density with depth for (a) ADCP 1 and (b) ADCP 4. z is the height above the bed and h is the water depth. The ratio z/h therefore indicates the relative height in the water column. The datasets presented here consist of the average power density over each tidal cycle. This removes the semi-diurnal variability to allow a clearer comparison between the specified depths over the whole time series.

Given the constraints on navigational clearance and avoiding the near surface region due to wave activity, it is desirable to place a turbine as high as possible in the water column. In the case of ADCP 4 (Fig. 19b), the spring power density increased by around 20% between $z/h = 0.4$ to $z/h = 0.6$, i.e. from 13 m to 20 m height above the bed. The large differences in the magnitude of spring tides in relation to the lunar synodic period is very clear in Fig. 19a, with power density increasing from 3 to 5 kW/m^2 during the two spring periods at $z/h = 0.8$ (around 31 m above the bed at mean sea level).

5.2. Wave-current interaction

The observations of WCI presented in section 4.5 have consequences on the operation of the Morlais site. The enhanced wave steepness encountered during the ebb tide will likely make device maintenance more challenging. Additionally, cyclic loading by waves can accelerate fatigue of the rotor and blades, and so should be considered at the design stage of the turbine [39].

As well as characterizing the wave conditions of a region, WCI can also alter tidal currents. The two main mechanisms involved in this process are wave-induced currents and enhanced bed friction. Wave-induced currents result from gradients in wave radiation stresses (e.g. due to wave breaking) [40]. This phenomenon is therefore a nearshore process and, while its effects may impinge into some shallower areas of the Morlais site closest to the shore, they are unlikely to be relevant [41].

Tidal currents and waves (provided the wave-induced orbital motions penetrate to a sufficient depth) experience shear stress with the sea bed. In environments where both waves and currents occur, the bed shear-stress that each experiences is enhanced by non-linear interaction in their respective boundary layers. Observations by Wolf and Prandle [34] demonstrated this effect on the current velocity, and similar results have been produced by numerical models [42]. A brief analysis, presented in Appendix B, concluded that wave-induced friction caused no significant reduction in current velocity at the Morlais site. A combination of more energetic waves and shallower water depths would be required for wave-induced orbital motions to penetrate with a sufficient velocity to the bed and noticeably enhance the bed shear stress.

6. Conclusion

After gathering together and processing data collected from and models developed of the commercial tidal stream site, Morlais, we find that depth averaged peak energy densities exceed 10 kW/m^2 during springs. Although there is significant wave-current interaction across the site, the main outcome of the interaction is modulation of the wave climate by the tidal currents, rather than any impact on the tidal power density. However, such modulation of the waves, particularly an increase in wave steepness, does add to the challenges of working in such a high energy environment, and has some implications for floating technologies. Although the origin of secondary flow features observed consistently across four ADCP moorings during the ebb phase of the tidal cycle has been speculated as eddies generated by a large bathymetric feature, more data collection or the development of a high resolution CFD (Computational Fluid Dynamics) model would be required to confirm their nature. However, since the secondary flows are below 1 m/s, they would likely be below the cut-in speed for a tidal energy convertor and would not affect energy conversion. With the construction of the sub-station, and the development of multiple tidal energy projects with Government (Contracts for Difference) support, the future at Morlais looks promising.

Acknowledgments

We are grateful to the captain and crew of the RV Prince Madog for many hours of multibeam surveys and successful deployment and recovery of the ADCP moorings. In addition, we thank the crew of the St. David for successful deployment and recovery of two of the moorings. We also thank Hydrowing, Magallanes and Mentor Môn for their role in deploying ADCPs in Morlais. We acknowledge the financial support of four European Regional Development Fund (ERDF) projects – SEACAMS 1 & 2 (Sustainable Expansion of the Applied Coastal and Marine Sectors), SEEC (Smart Efficient Energy Centre), and MEECE (Marine Energy Engineering Centre of Excellence). We also acknowledge the support of NERC (Natural Environment Research Council) project NE/V009109/1. Finally, we thank the three anonymous reviewers who provided constructive criticisms on an earlier version of the manuscript

Data availability

The data used in this publication will be made available on reasonable request.

Appendix A. Additional plots of ADCP data

The probability histograms of U_{mean} for each of the ADCP deployments is given in Fig. A.20.

Appendix B. WCI: The effect of waves on current velocity

The total shear stress that an ocean current experiences with the bed comes from three contributions: skin friction, form drag and drag induced by suspended sediment. Skin friction is caused by interaction between fluid in motion and the sediment grains, and thus larger grains enhance this contribution. Form drag results from pressure gradients which emerge when the current passes bed features (e.g. sand ripples or submerged objects). Lastly, should the skin friction reach a sufficient level (quantified by the *entrainment velocity*), sediment becomes suspended in the water column. In this process, some momentum is transferred from the current to the sediment grains.

An estimate of how the current shear stress due to skin friction alone is modified by the presence of waves can be determined using the relationships given in Soulsby [32]. Most notable is the following expression, which determines the combined shear stress due to waves and current

$$\tau_m = \tau_c \left[1 + 1.2 \left(\frac{\tau_w}{\tau_c + \tau_w} \right)^{3.2} \right] \tag{B.1}$$

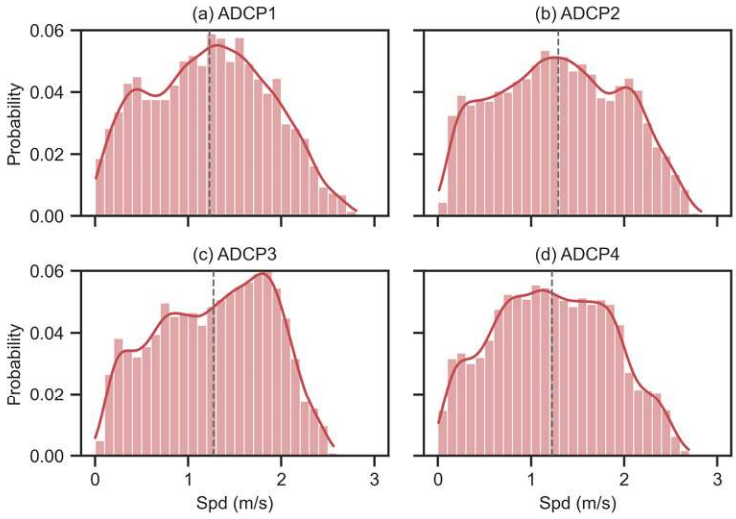

Figure A.20: Probability histograms of depth-averaged current speed (U_{mean}) for the four ADCP deployments. The solid red line on each plot is the kernel density estimate (KDE), and the dashed line is the mean.

where τ_w and τ_c are the wave and current-only shear stresses, respectively, and τ_m is the mean combined shear stress. The following relation for a monochromatic wave provides further insight

$$U_w = \frac{\pi H}{T \sinh(kh)} \tag{B.2}$$

where U_w is the near-bed velocity of the wave-induced orbital motions, H is the wave height, T the period, k is the wavenumber, and h is water depth (Fig. B.21).

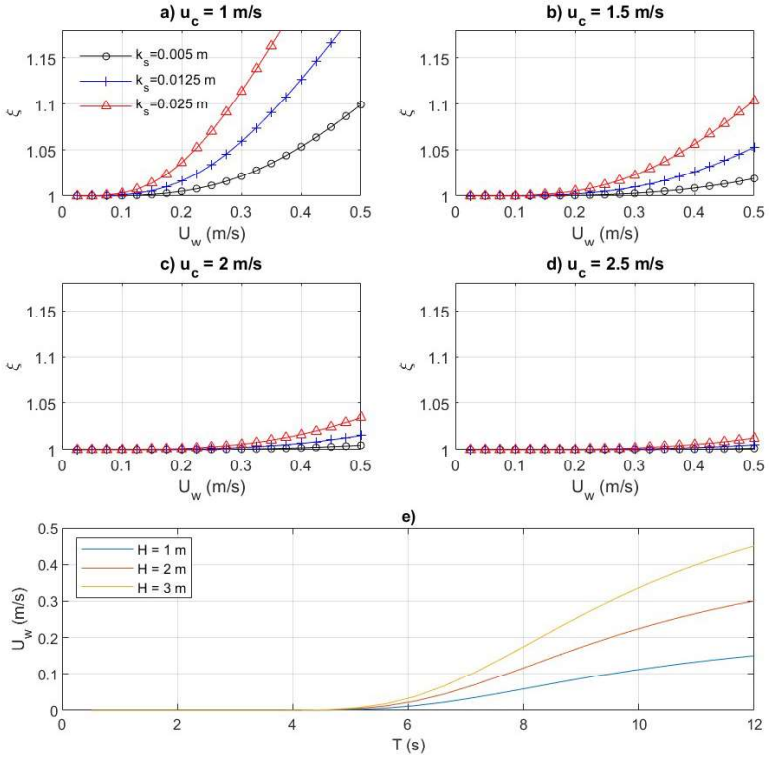

Figure B.21: (a-d) The relationship between near-bed orbital velocity (U_w) and the ratio of the enhanced (due to waves) drag coefficient to current-only drag coefficient (ξ) for a monochromatic wave, across four depth-averaged current speeds (u_c) and three Nikuradse bed roughnesses values (k_s) (approximating grain diameters of 2 mm ($k_s = 0.005$), 5 mm ($k_s = 0.0125$)) and 10 mm ($k_s = 0.025$)). (e) The resulting U_w across a range of T and three wave heights H. Adapted from [41].

The analysis presented in Fig. B.21 is limited by the fact that it considers only (1) the skin friction component of shear stress and (2) it is for monochromatic waves. While this limits its application to actual predictions, it does highlight that stronger tidal flows (i.e. those that occur at tidal energy sites) are less impacted by wave-induced currents than weaker flows. Also apparent, is that waves with both a large height and period are required to make any significant alteration to the shear stress experienced by the flow. For this reason, the following variable is introduced for this analysis in an attempt to examine the effects of the lower frequency (swell) components of the wave spectrum in isolation [43]

$$H_{s,\mathrm{swell}} = 4\sqrt{\int_0^{2\pi}\int_0^{\sigma_{\mathrm{swell}}} E(\sigma,\theta)\,d\sigma\,d\theta} \tag{B.3}$$

where σ_{swell} is the intrinsic swell radian frequency, E is the wave energy spectrum and θ is the wave direction. This is almost identical to the procedure for obtaining the significant wave height, however, the integration is only performed over frequencies lower than 0.1 Hz (those associated with swell waves).

While any wave-induced increases in shear stress at Morlais would result from the combination of a spectrum of wave frequencies, and may include significant contributions from the two other forms of bed shear stress, this analysis suggests that the site is too deep for waves to influence bed friction.

The examination of wave-induced changes in current velocity are complicated by one significant factor. Namely, any effects of waves on the current velocity are likely to be small, meaning that their co-occurrence with the (much more notable) wave modifications makes observing them difficult. Any correlation analysis between a wave property (e.g. wave height) and current speed will likely only display modification of the waves by the current.

In order to observe the effects of waves on the current, therefore, the tidal signal (possessing the frequency at which the current would be modifying the waves) would have to be removed. This was achieved by using the MATLAB package `t_tide` to produce a tidal prediction of the U_{mean} during the deployment period of ADCPs 1 and 4 and subtracting it from the observed U_{mean}. This resulting time series is termed the residual velocity. The frictional influence of waves will cause this value to be more negative.

The residual velocity (which captured 97.1% and 97.7% of the variability in current speed at ADCP 1 and 4 respectively) was then plotted against the two measures of wave height (Fig. B.22).

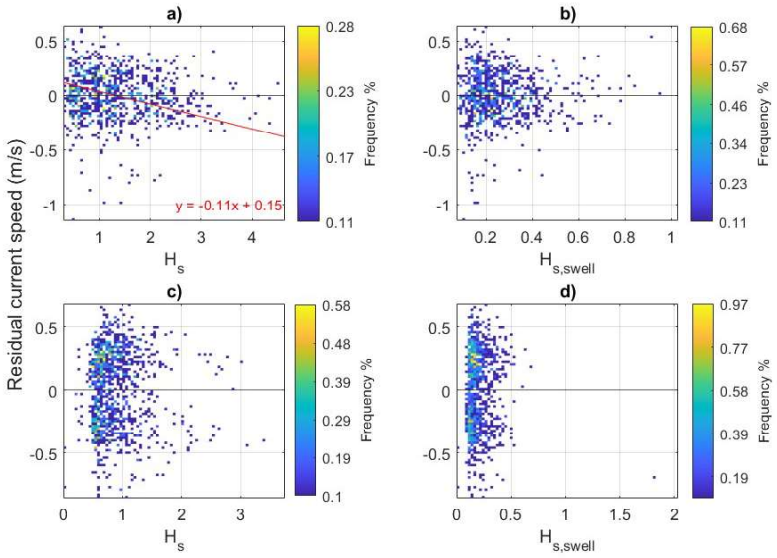

Figure B.22: Examination of the relationship of both (a,c) H_s and (b,d) $H_{s,swell}$ with the residual current at ADCP 1 (a,b) and 4 (c,d). Any wave-induced frictional effects on the current velocity would be expressed as a negative residual current speed, which would be expected to reduce linearly with greater wave height [34][42]. A statistically significant negative relationship was present between H_s and the residual current speed at ADCP 1 only ($P = 0.0015$). The residual current speed at ADCP 4 was significantly influenced by the severe inability of the tidal prediction to capture the tidal asymmetry at this mooring, hence the flood always exceeded the prediction and the ebb never reached it.

The statistically significant relationship in Fig. B.22 brings into question whether it is the waves having an influencing effect on the residual current or vice versa.

Recall that the residual current speed is purely a measure of how the observed current speed differed from the tidal prediction. As the tidal prediction was unable to fully capture the tidal asymmetry at either mooring (underestimating the flood and overestimating the ebb, most notably at ADCP 4), this would result in a negative current residual generally occurring during the ebb (as the observations were less than the prediction) and a positive one during the flood (observations greater than prediction). From this, it would be expected that the increased wave height caused by the ebb tide (Fig. 17) would approximately occur with a negative current residual.

In observing the measured current speed next to the tidal prediction, it was at peak tides that the disparity was greatest. For this reason, it cannot be said with any certainty that the effects of waves on current speed are being observed in Fig. B.22. It seems likely, considering the relatively quiescent wave climate

of the region and its water depth, that the these effects are minimal at Morlais, and that the inverse is being observed in Fig. B.22.

References

[1] UNFCCC, The Paris Agreement (2015).
URL https://unfccc.int/process-and-meetings/the-paris-agreement

[2] UK Government, Uk enshrines new target in law to slash emissions by 78% by 2035 (Apr 2021).
URL https://www.gov.uk/government/news/uk-enshrines-new-target-in-law-to-slash-emissions-by-78-by-2035

[3] National Grid, How much of the uk's energy is renewable? (2023).
URL https://www.nationalgrid.com/stories/energy-explained/how-much-uks-energy-renewable

[4] S. P. Neill, K. A. Haas, J. Thiébot, Z. Yang, A review of tidal energy—resource, feedbacks, and environmental interactions, Journal of Renewable and Sustainable Energy 13 (6) (2021).

[5] S. P. Neill, A. Vögler, A. J. Goward-Brown, S. Baston, M. J. Lewis, P. A. Gillibrand, S. Waldman, D. K. Woolf, The wave and tidal resource of scotland, Renewable Energy 114 (2017) 3–17. doi:https://doi.org/10.1016/j.renene.2017.03.027.
URL https://www.sciencedirect.com/science/article/pii/S0960148117302082

[6] S. P. Neill, I. A. Fairley, S. Rowlands, S. Young, T. Hill, C. A. Unsworth, N. King, M. J. Roberts, M. J. Austin, P. Hughes, I. Masters, A. Owen, B. Powell, D. E. Reeve, M. J. Lewis, Characterizing the marine energy test area (meta) in wales, uk, Renewable Energy 205 (2023) 447–460. doi:https://doi.org/10.1016/j.renene.2023.01.105.

[7] Tidal clients: European marine energy centre.
URL https://www.emec.org.uk/about-us/our-tidal-clients/

[8] I. G. Bryden, Tidal energy, in: C. J. Cleveland (Ed.), Encyclopedia of Energy, Elsevier, New York, 2004, pp. 139–150. doi:https://doi.org/10.1016/B0-12-176480-X/00342-9.
URL https://www.sciencedirect.com/science/article/pii/B012176480X003429

[9] S. Draper, T. A. Adcock, A. G. Borthwick, G. T. Houlsby, Estimate of the tidal stream power resource of the Pentland Firth, Renewable Energy 63 (2014) 650–657. doi:https://doi.org/10.1016/j.renene.2013.10.015.

[10] Meygen.
URL https://saerenewables.com/tidal-stream/meygen/

[11] UKMEC, News, events and little bit about what we do | UK Marine Energy Council (UKMEC) (2022).
URL https://www.marineenergycouncil.co.uk/news/year:2022

[12] The morlais story.
URL https://www.morlaisenergy.com/en/about-us/the-morlais-story

[13] S. P. Neill, Wave resource characterization and co-location with offshore wind in the irish sea, Renewable Energy 222 (2024) 119902.

[14] Contracts for difference (cfd) allocation round 5: results.
URL https://www.gov.uk/government/publications/contracts-for-difference-cfd-allocation-round-5-results

[15] D. for, Contracts for difference (cfd) allocation round 6: results (Sep 2024).
URL https://www.gov.uk/government/publications/contracts-for-difference-cfd-allocation-round-6-results

[16] I. Fairley, P. Evans, C. Wooldridge, M. Willis, I. Masters, Evaluation of tidal stream resource in a potential array area via direct measurements, Renewable Energy 57 (2013) 70–78. doi:https://doi.org/10.1016/j.renene.2013.01.024.
URL https://www.sciencedirect.com/science/article/pii/S0960148113000499?via%3Dihub

[17] M. Piano, S. Neill, M. Lewis, P. Robins, M. Hashemi, A. Davies, S. Ward, M. Roberts, Tidal stream resource assessment uncertainty due to flow asymmetry and turbine yaw misalignment, Renewable Energy 114 (2017) 1363–1375. doi:https://doi.org/10.1016/j.renene.2017.05.023.
URL https://www.sciencedirect.com/science/article/pii/S0960148117304081

[18] Substation construction for morlais tidal energy project wraps up.
URL https://www.offshore-energy.biz/

[19] Successful handover (2024).
URL https://www.morlaisenergy.com/en/news/latest-news/successful-handover-2024-02-01

[20] Successful environmental plan (2024).
URL https://www.morlaisenergy.com/en/news/latest-news/successful-environmental-plan-2024-09-13

[21] S. P. Neill, A. J. Elliott, M. R. Hashemi, A model of inter-annual variability in beach levels, Continental Shelf Research 28 (14) (2008) 1769–1781.

[22] M. Togneri, I. Masters, Micrositing variability and mean flow scaling for marine turbulence in ramsey sound, Journal of Ocean Engineering and Marine Energy 2 (1) (2015) 35–46. doi:https://doi.org/10.1007/s40722-015-0036-0.

[23] N. Booij, R. C. Ris, L. H. Holthuijsen, A third-generation wave model for coastal regions: 1. model description and validation, Journal of Geophysical Research: Oceans 104 (C4) (1999) 7649–7666.

[24] H. Hersbach, B. Bell, P. Berrisford, S. Hirahara, A. Horányi, J. Muñoz-Sabater, J. Nicolas, C. Peubey, R. Radu, D. Schepers, et al., The ERA5 global reanalysis, Quarterly Journal of the Royal Meteorological Society 146 (730) (2020) 1999–2049.

[25] G. D. Egbert, S. Y. Erofeeva, Efficient inverse modeling of barotropic ocean tides, Journal of Atmospheric and Oceanic Technology 19 (2) (2002) 183–204.

[26] M. Lewis, S. Neill, P. Robins, M. Hashemi, Resource assessment for future generations of tidal-stream energy arrays, Energy 83 (2015) 403–415.

[27] K. J. Van Landeghem, A. J. Wheeler, N. C. Mitchell, Seafloor evidence for palaeo-ice streaming and calving of the grounded irish sea ice stream: implications for the interpretation of its final deglaciation phase, Boreas 38 (1) (2009) 119–131.

[28] P. E. Robins, S. P. Neill, M. J. Lewis, S. L. Ward, Characterising the spatial and temporal variability of the tidal-stream energy resource over the northwest european shelf seas, Applied Energy 147 (2015) 510–522.

[29] D. Pugh, P. Woodworth, Sea-Level Science: Understanding Tides, Surges, Tsunamis and Mean Sea-Level Changes, Vol. 407, Cambridge University Press, 2014.

[30] S. P. Neill, The role of coriolis in sandbank formation due to a headland/island system, Estuarine, Coastal and Shelf Science 79 (3) (2008) 419–428.

[31] S. P. Neill, M. R. Hashemi, M. J. Lewis, The role of tidal asymmetry in characterizing the tidal energy resource of orkney, Renewable Energy 68 (2014) 337–350.

[32] R. Soulsby, Dynamics of marine sands (1997).

[33] M. Lewis, S. Neill, P. Robins, M. Hashemi, S. Ward, Characteristics of the velocity profile at tidal-stream energy sites, Renewable Energy 114 (2017) 258–272. doi:https://doi.org/10.1016/j.renene.2017.03.096.
URL https://www.sciencedirect.com/science/article/pii/S0960148117302884

[34] J. Wolf, D. Prandle, Some observations of wave–current interaction, Coastal Engineering 37 (3-4) (1999) 471–485. doi:https://doi.org/10.1016/s0378-3839(99)00039-3.

[35] M. R. Hashemi, S. P. Neill, The role of tides in shelf-scale simulations of the wave energy resource, Renewable Energy 69 (2014) 300–310.

[36] S. P. Neill, J. R. Jordan, S. J. Couch, Impact of tidal energy converter (tec) arrays on the dynamics of headland sand banks, Renewable Energy 37 (1) (2012) 387–397.

[37] T. A. A. Adcock, S. Draper, G. T. Houlsby, A. G. L. Borthwick, S. Serhadlıoğlu, The available power from tidal stream turbines in the pentland firth, Proceedings of the Royal Society A: Mathematical, Physical and Engineering Sciences 469 (2157) (2013) 20130072. doi:https://doi.org/10.1098/rspa.2013.0072.

[38] P. E. Robins, S. P. Neill, M. J. Lewis, Impact of tidal-stream arrays in relation to the natural variability of sedimentary processes, Renewable Energy 72 (2014) 311–321.

[39] X. Guo, J. Yang, Z. Gao, T. Moan, H. Lu, The surface wave effects on the performance and the loading of a tidal turbine, Ocean Engineering 156 (2018) 120–134. doi:https://doi.org/10.1016/j.oceaneng.2018.02.033.

[40] M. Longuet-Higgins, R. Stewart, Radiation stresses in water waves; a physical discussion, with applications, Deep Sea Research and Oceanographic Abstracts 11 (4) (1964) 529–562. doi:https://doi.org/10.1016/0011-7471(64)90001-4.

[41] M. R. Hashemi, S. P. Neill, P. E. Robins, A. G. Davies, M. J. Lewis, Effect of waves on the tidal energy resource at a planned tidal stream array, Renewable Energy 75 (2015) 626–639. doi:https://doi.org/10.1016/j.renene.2014.10.029.
URL https://www.sciencedirect.com/science/article/pii/S0960148114006569

[42] M. Lewis, S. Neill, M. Hashemi, M. Reza, Realistic wave conditions and their influence on quantifying the tidal stream energy resource, Applied Energy 136 (2014) 495–508. doi:https://doi.org/10.1016/j.apenergy.2014.09.061.

[43] User manual, swan cycle iii version 41.51. doi:https://swanmodel.sourceforge.io/online_doc/swanuse/node35.html.